POAC'25
St. John's, Newfoundland and Labrador, Canada

Proceedings of the 28th International Conference on Port and Ocean Engineering under Arctic Conditions
Jul 13-17, 2025
St. John's, Newfoundland and Labrador
Canada

Application of the Material Point Method for Simulating Sea Ice Breakup

Igor Gribanov[1], Takuji Waseda[1], Rocky Taylor[2], Ian Turnbull[3]
[1] University of Tokyo, Kashiwa, Chiba, Japan
[2] Memorial University of Newfoundland, St.John's, Newfoundland and Labrador, Canada
[3] C-CORE, St.John's, Newfoundland and Labrador, Canada

ABSTRACT

Nares Strait is a major pathway for the thick multi-year ice to leave the Arctic Ocean. The Material Point Method (MPM) is applied to simulate the breakup of sea ice in Nares Strait, a key region for Arctic sea ice loss. Traditional numerical methods, such as the Finite Element Method (FEM) and Discrete Element Method (DEM), face challenges in handling large deformations and fracture propagation in ice modeling. MPM, which combines particle- and grid-based representations, overcomes these limitations by naturally supporting deformation and progressive failure. The study models the ice breakup process using a high-resolution MPM implementation, capturing interactions between ice and ocean currents. The breakup occurs primarily in regions of high stress concentration, such as around islands and narrow passages, consistent with observed satellite imagery. However, discrepancies remain as the simulation does not fully capture all natural forces. The results highlight MPM's potential for advancing sea ice modeling and improving predictions of ice dynamics.

KEY WORDS: Numerical Modelling, Material Point Method, Sea Ice Dynamics.

INTRODUCTION

Sea ice in the Arctic and Antarctic plays a vital role in regulating the global climate and ocean circulation. As climate change causes ice to melt and shift more rapidly, accurate modeling and forecasting are essential for understanding its effects on weather patterns, marine navigation, and coastal communities. Numerical models, such as CICE (Los Alamos Sea Ice Model), are designed to capture the prominent physical phenomena, e.g., the fracture and the motion of sea ice. Reanalysis systems combine real-world measurements with simulations to improve accuracy and fill in gaps where observations are missing, creating more reliable datasets for studying sea ice changes. These systems are designed to cover large geographical areas, such as the entire Arctic or Antarctic region, and, as a result, often have low to moderate spatial resolution. For example, TOPAZ4b has a spatial resolution of 3x3 km (European Union-Copernicus Marine Service, 2020).

In some cases, it is preferable to work with models that capture a higher level of detail. Processes such as ridge formation, fragmentation, arching, changes in pressure distribution, and the motion of ice cover during breakup present both practical and academic interest. Common methods for modeling ice motion include the Finite Element Method (FEM) and the Discrete Element Method (DEM). FEM provides high flexibility in handling complex geometries and boundary conditions, making it ideal for modeling ice deformation and interactions with structures. However, its computational cost is high, limiting its scalability. Difficulties arise when many fragments interact, requiring computationally intensive collision detection. DEM, on the other hand, represents ice as discrete particles, making it suitable for simulating ice breakup and rafting (Åström et al., 2024; Polojärvi, 2022). However, DEM requires extensive calibration and has difficulties with representing fragments whose size is smaller than the element size.

In this work, we apply the Material Point Method, which uses both particles and a grid for computation. It is well-suited for ice modeling because it can accurately capture the large deformations, fracture, and ridge formation that characterize sea ice behavior. Unlike traditional grid-based methods, MPM represents ice as material points moving through a background grid, allowing it to handle complex ice dynamics without the limitations of fixed-mesh approaches. Since MPM naturally supports the inclusion of irrecoverable deformation and progressive material failure, it can model evolving damage and fragmentation of ice under external forces like wind and ocean currents.

Observations in Nares Strait

The simulation is based on the Nares Strait location. This narrow passage between Greenland and Canada (~600 km long and ~4-80 km wide) plays a crucial role in Arctic ice dynamics and ocean circulation and exhibits complex ice behavior like arches, polynyas, and seasonal ice jams (Moore et al. 2023). While this work does not aim to accurately reproduce all these processes, the existing research about the area helps to identify the prominent phenomena and set up the simulation.

Nares Strait has been extensively studied to understand its ice and ocean current dynamics. Several measurements have been made in the region, particularly focusing on ice concentration and flow velocity. Satellite imagery and in situ observations have provided estimates of ice flux, with an annual volume of approximately 141 km³ being transported through the Strait (Kwok et al., 2010).

According to Kirillov et al. (2021) the mean southerly current velocity in the surface layer of Kennedy Channel is about 0.15 ± 0.04 m/s, whereas the near-surface lunar semidiurnal tidal amplitudes range is 0.22–0.24 m/s. Tidal currents induce periodic reversals and can temporarily halt or even reverse ice drift under certain wind conditions. The pack ice in the Channel drifts faster than the current, with a mean speed of up to 0.23 m/s (Kwok, 2005), which is thought to be a result of additional wind stress.

Ice breakup in Nares Strait is primarily caused by a combination of oceanic heat flux, wind forcing, and tidal effects. The formation of polynyas, such as the North Open Water (NOW) polynya, plays a crucial role in weakening ice structures. Oceanic heat flux from warmer Atlantic and Pacific waters has been observed to create areas of thinner ice, particularly along the western coast of the Strait, facilitating earlier breakup. Additionally, changes in wind

patterns and increasing temperatures due to climate change have been linked to a decline in the stability of ice arches that historically blocked ice movement (Kirillov et al., 2021).

In situ observations of ice thickness in the Lincoln Sea show a typical modal thickness of 3.5–4.3 m for multi-year ice (MYI) and around 2.2 m for first-year ice (FYI) (Haas et al., 2017; Lange et al., 2019). TOPAZ5 reanalysis dataset estimates the ice thickness in Kennedy Channel in the range 0.5-1.5 m on June 10, 2024.

Figure 1 shows ice conditions in Nares Strait throughout 2024, ranging from the intact cover to the breakup period and low ice concentration. During that year, the first signs of breakup appear on June 8-10, and by June 20, the ice cover is fragmented.

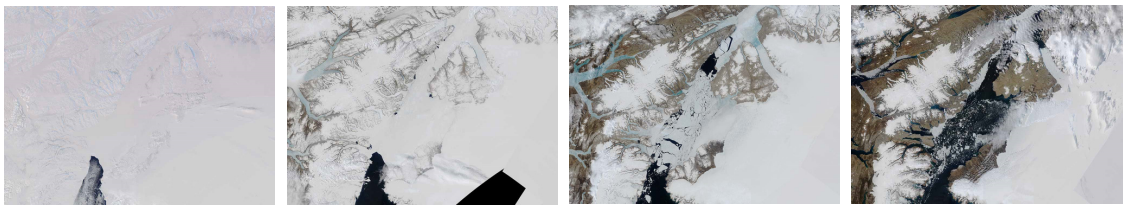

(a) April 8, 2024 (b) June 8, 2024 (c) June 20, 2024 (d) August 10, 2024

Figure 1. Satellite image of ice conditions in Nares Strait ("Copernicus Sentinel-2 satellite imagery," 2024).

METHOD FORMULATION

The Material Point Method (MPM) models deformable materials by using discrete material points that carry physical properties such as mass, velocity, position, and deformation gradient (Nguyen et al., 2023). These points do not interact directly but instead rely on a background computational grid to handle forces and motion updates. By combining particle and grid representations, MPM enables the modeling of deformable materials without the typical issues of purely mesh-based or particle-based methods.

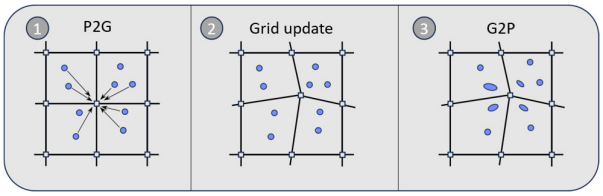

Figure 2. Computation steps of the Material Point Method (MPM).

Several variants exist within the family of material point methods. We utilize the Moving Least Squares (MLS) formulation outlined by Hu et al. (2018) as it provides good accuracy when modelling solids and granular materials. The computational cycle starts with the Particle-to-Grid (P2G) transfer (Figure 2), where particles' mass and momentum are mapped to the background grid using the shape function (or weight function). Stress values are calculated per point and transferred onto the grid in the form of additional impulses on grid nodes (Hu et al., 2018):

$$\Delta \mathbf{p}_i = -\sum_p \omega_{ip}\, V_p^0\, M_p^{-1}\, J\, \boldsymbol{\sigma}\left(\mathbf{F}_p^E\right)\left(\boldsymbol{x}_i - \boldsymbol{x}_p\right)\Delta t, \tag{1}$$

where ω_{ip} is the weight function value between the node i and the point p, V_p^0 is the initial volume associated with the point, M_p^{-1} is a constant that depends on the cell size, $\mathbf{F}_p^E$ is the deformation gradient (its elastic component) associated with the point, $J = \det(\mathbf{F}_p^E)$, $\boldsymbol{x}_p$ is the position of the point, $\boldsymbol{x}_i$ is the position of the grid node, Δt is the time step, and $\boldsymbol{\sigma}(\mathbf{F}_p^E)$ is the Cauchy stress.

Equation (1) provides some flexibility for the constitutive model of the material. Typically, points are distributed uniformly in space and have identical initial volumes V_p^0. However, in the 2D case, the thickness of the modelled layer can be represented as varying V_p^0 values for each point. In a state of static equilibrium, variations in the material's thickness result in variations in stress values. Consequently, thinner areas serve as stress concentrators where fractures initiate.

External forces and boundary conditions are applied at the second step of the computation cycle, known as the grid update. Nodes that are outside of the modelled domain, e.g., land mass, have their momentum set to zero. In this work, an ocean current creates external drag forces, which are applied to nodes. Nodal velocities are computed during the grid update.

Points are advected at the concluding computational step, Grid-to-Particle (G2P) transfer. This step alters the point's deformation gradient as follows:

$$\mathbf{F}_p^{n+1} = (\mathbf{I} + \Delta t \nabla \mathbf{v}) \mathbf{F}_p^n, \tag{2}$$

where $\nabla \mathbf{v}$ is the spatial gradient of the velocity field. When modelling elastic solids, this operation would conclude the computation cycle. However, to represent rubble formation, crushing, and tensile fracture, additional operations are required at this stage.

Plasticity Model

The deformation gradient from expression (2) can be viewed as a product of the elastic and plastic parts:

$$\mathbf{F} = \mathbf{F}^E \mathbf{F}^P. \tag{3}$$

Here, $\mathbf{F}$ denotes the deformation gradient $\mathbf{F}_p^{n+1}$ from expression (2). For simplicity, we drop the subscript and the superscript. Initially, there is no plastic deformation in the material, and the plastic part $\mathbf{F}^P$ is set to identity. We treat solid ice as purely elastic material, where $\mathbf{F}^E$ is used to compute the Cauchy stress $\boldsymbol{\sigma}(\mathbf{F}^E)$. In certain conditions, a fracture criterion is imposed to distinguish the intact solid ice from the material that was fractured in some way. The criterion is based on the elliptical failure envelope in p-q space suggested by Derradji-Aouat (2003, 2000). Figure 3 shows the failure envelope, where p denotes the hydrostatic pressure and q denotes the deviatoric stress measure, von Mises stress. The envelope is based on experimental data, although its parameters may vary depending on the type of ice and the strain rate. The criterion works best in real-life situations of multiaxial loading where most fractures happen in shear.

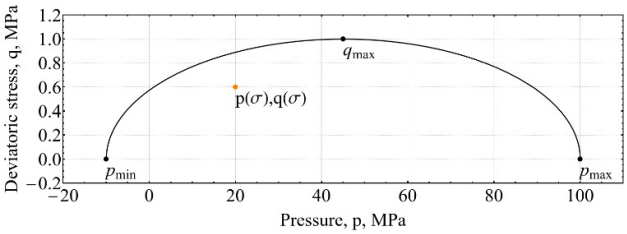

Figure 3. Elliptical failure envelope in p-q space.

To apply this criterion, we take the updated deformation gradient $\mathbf{F}^E$ for each point and recompute the stress value $\boldsymbol{\sigma}(\mathbf{F}^E)$ using the Neo-Hookean expression:

$$\boldsymbol{\sigma}(\mathbf{F}^E) = \mu J^{-\frac{2}{d}-1}\,\mathrm{dev}(\mathbf{F}^E(\mathbf{F}^E)^T) + \frac{\kappa}{2}\left(J - \frac{1}{J}\right)\mathbf{I}, \tag{4}$$

where μ is shear modulus, κ is the bulk modulus, d is the dimension of the problem, $\mathrm{dev}(\mathbf{F}^E(\mathbf{F}^E)^T)$ denotes the deviatoric part of $\mathbf{F}^E(\mathbf{F}^E)^T$, and $J = \det(\mathbf{F}^E)$. For the material considered, all elastic deformations are small, on the order or <0.01% and the expression yields similar results as the Hooke's Law. The two terms of expression (4) correspond to the effects of the shear deformation and the bulk deformation. Using the standard definitions, one can obtain the expressions for hydrostatic pressure and deviatoric stress:

$$\begin{aligned} p &= -\frac{\kappa}{2}(J^2 - 1), \\ q &= \sqrt{\frac{6-d}{2}}\,\mu J^{-\frac{2}{d}}\,\|\mathrm{dev}(\mathbf{F}^E(\mathbf{F}^E)^T)\|. \end{aligned} \tag{5}$$

Expressions (5) are derived from the Kirchhoff stress $\boldsymbol{\tau} = J\boldsymbol{\sigma}$.

Having computed the values p and q, we check whether they fall outside of the elastic region (Figure 3). Should this happen, the point will be marked as "fractured" and plastic yield will be applied from then on. The exact fracture mechanism is not considered, but the material changes its behavior to granular. Its ability to sustain tensile stress is greatly reduced (to zero or near-zero values), whereas shear stress can be sustained only in combination with hydrostatic pressure. Such behavior is adequately described by the Drucker-Prager yield criterion, and we apply its modified version.

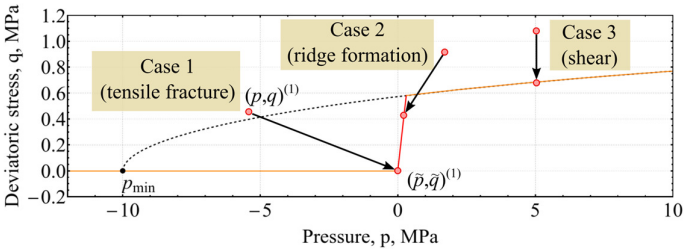

Figure 4. Yield surface and three cases of the plasticity update.

Plastic deformation can be categorized into three distinct cases (Figure 4) – tensile fracture, rubble formation in compression, and shear deformation of the ridges.

Case 1: In tension, the material is allowed to expand freely This case is characterized by negative pressure ($p < 0$). The values of p and q are projected to the new values of $\tilde{p} = 0$ and $\tilde{q} = 0$. The material does not sustain any stress and yields easily, which roughly corresponds to dispersing the broken ice in the surrounding water. Plastic deformation does not change the total deformation gradient $\mathbf{F}$, but transforms its constituent elastic and plastic components $\mathbf{F}^E$ and $\mathbf{F}^P$ into the updated $\tilde{\mathbf{F}}^E$ and $\tilde{\mathbf{F}}^P$.

$$\mathbf{F} = \mathbf{F}^E\mathbf{F}^P = \tilde{\mathbf{F}}^E\tilde{\mathbf{F}}^P. \tag{6}$$

In Case 1, the updated elastic part $\tilde{\mathbf{F}}^E$ becomes the identity, therefore all deformation goes into the plastic portion: $\tilde{\mathbf{F}}^P = \mathbf{F}^E\mathbf{F}^P$. In practice, the simulation does not preserve the value of the plastic portion of the deformation gradient. However, it is useful to keep track of its determinant, which reflects the change in volume attributed to plastic deformation:

$$J_p^{-1} = \det(\mathbf{F}^P)^{-1}. \tag{7}$$

In material that undergoes plastic stretching, the value will be lower than one: $J_p^{-1} < 1$. For numerical stability, it also helps to limit the amount of stretching to a small positive value, such as 0.1. It is noted that in the physical ice system under tension, the ice does not plastically stretch, but rather the localized break-up and dispersion of broken ice reduces the concentration of ice of given thickness in that region. So while in the physical system the actual thickness of the individual ice fragments does not change, this localized reduction in concentration of ice under divergent conditions results in a lower average ice thickness for that region. Thus the analogy of plastic stretching in the model is seen as quite reasonable since localized decreases in mean ice thickness due to irrecoverable deformations occur in the pack.

Case 2: Similarly to stretching, the material is allowed to undergo plastic compression in some cases. In a normal 3D scenario a non-porous material would not undergo plastic compression. However, for a 2D layer of ice, such compression is physically representative of an increase of the thickness of the layer and the formation of ridges. Similarly to Case 1, we limit the value of J_p^{-1} to a pre-defined value (in the current model it is set to 3), setting the limit to the growth of ridges.

Case 3: Material that is under hydrostatic pressure ($p > 0$) and a shear stress that exceeds the yield limit, undergoes plastic shear deformation. In this case, the value of p remains unchanged, while q is projected onto the yield surface (Figure 4) to become an updated non-zero $\tilde{q}$. The change is reflected in the updated values of $\tilde{\mathbf{F}}^E$ and $\tilde{\mathbf{F}}^P$ as per Wolper et al. (2021). Physically, this corresponds to a situation where rubble shifts in shear, relieving stress, but preserving the ability to elastically deform under lower loads.

Our implementation is written in CUDA C++ and leverages GPUs for efficient computation (https://github.com/igorg520b/iceMPM_2d_sp). The computation is performed in double-precision arithmetic, and we improve accuracy by adding an integer cell index to describe the position of a point.

SIMULATION SETUP

This work focuses on the Nares Strait area, including Kane Basin, Kennedy Channel, and Hall Basin. The area includes Hans Island, Crozier Island, and Franklin Island, which are obstacles

to the current and ice movement. Natural processes that participate in the ice breakup are rather complex and include melting, wind drag, and current drag. The current is influenced by many factors, including tidal currents. For a numerical simulation, a high-resolution forcing field is important. For example, the current flow around the islands would cause stress concentrations and, likely, fragmentation of ice. In this work, we chose to consider only the current drag force as the driver of the breakup. Moreover, we model it as a steady southward flow in a 2D channel with a given volume transport. While such an approach is not an accurate representation of the complex natural currents, it provides an approximation with smooth streamlines (constant depth), which works best for the numerical setup (Figure 5a). The modelled region coincides with the region where the flow is modelled. All other areas are considered as landmass with zero velocity boundary conditions.

The initial ice cover, represented by material points, is initialized from the satellite image (Figure 5b). Pixels' color is used to distinguish between open water and solid ice. Color variations often follow ridges, refrozen cracks, or existing cracks, which serve as stress concentrators. To introduce randomness into the simulated material we use color to set the thickness to range from 0.8 m to 1.0 m (although this is not intended to measure the actual thickness). Color codes corresponding to water and varying thickness are shown in Figure 5b.

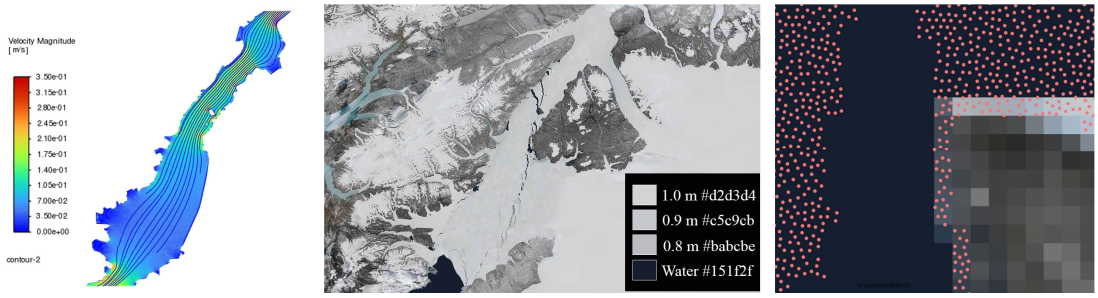

(a) (b) (c)

Figure 5. (a) Modelled flow velocity field in the strait; (b) Sentinel-2 satellite image taken on June 10, 2024 of Nares Strait is used to initialize the simulation ("Copernicus Sentinel-2 satellite imagery," 2024); (c) Distribution of material points in the simulation, 1 × 1 km area near Franklin Island is shown. Blue background indicates the modelled area where particles are free to move.

The simulation uses explicit integration with a fixed time step. Modelled area is a rectangle measuring 430 × 285 km with the corresponding grid resolution of 14,895 × 9,856 (the active modelled area is 7,184 × 9,856). The simulation does not consider the earth's curvature. Cell size is 28.9 m. Initially, there are five material points per cell, distributed via Poisson disk sampling, which is a non-structured distribution. Figure 5c shows a 1 × 1 km region near Franklin Island with individual material points. Blue background indicates open water. Some overlap between the points and the land boundary is acceptable.

Simulation parameters are summarized in Table 1. Grid resolution and material point count are selected to fit within our hardware constraints (24GB of RAM). Five points per cell is the parameter suggested in the literature (Nguyen et al., 2023). The mechanical parameters of ice come from the literature. A lower value of Young's Modulus is selected to increase the time step, which is a common technique in numerical modelling. The failure envelope parameters are based on the work by Derradji-Aouat (2000, 2023). The time step is selected to satisfy the Courant-Friedrichs-Lewy (CFL) condition.

Table 1. Simulation parameters

Parameter	Notation	Value
Simulated area		430 × 285 km
Grid resolution		14,895 × 9,856
Grid cell size	h	28.9 m
Initial points per cell		5 (average)
Time step	Δt	0.026 s
Ice density	ρ	916 kg/m^3
Initial ice cover thickness		0.8 – 1.0 m
Young's modulus	E	0.5 GPa
Poisson ratio	ν	0.3
Failure envelope range	p_{min}, p_{max}	-10, 100 MPa
Shear strength		2.5 MPa
Number of points		102 million
Simulated time		18 hours

RESULTS

The simulation ran 2.5 million time steps, covering an 18-hour period. During that time, a substantial breakup of ice cover occurred, and the floes traveled as far as 20 km. Figure 6 shows the final configuration of the ice cover and the end of the simulation. Fractured material is allowed to compress (and expand) plastically, and the associated surface density change J_p^{-1} is highlighted. Red colors indicate the formation of ridges, while the traces of blue color indicate the fracture and dispersal of the material at the newly created boundaries. The simulated hydrostatic pressures reach as high as 500 kPa (not shown in the figure). Overall, the ice cover follows the southward current.

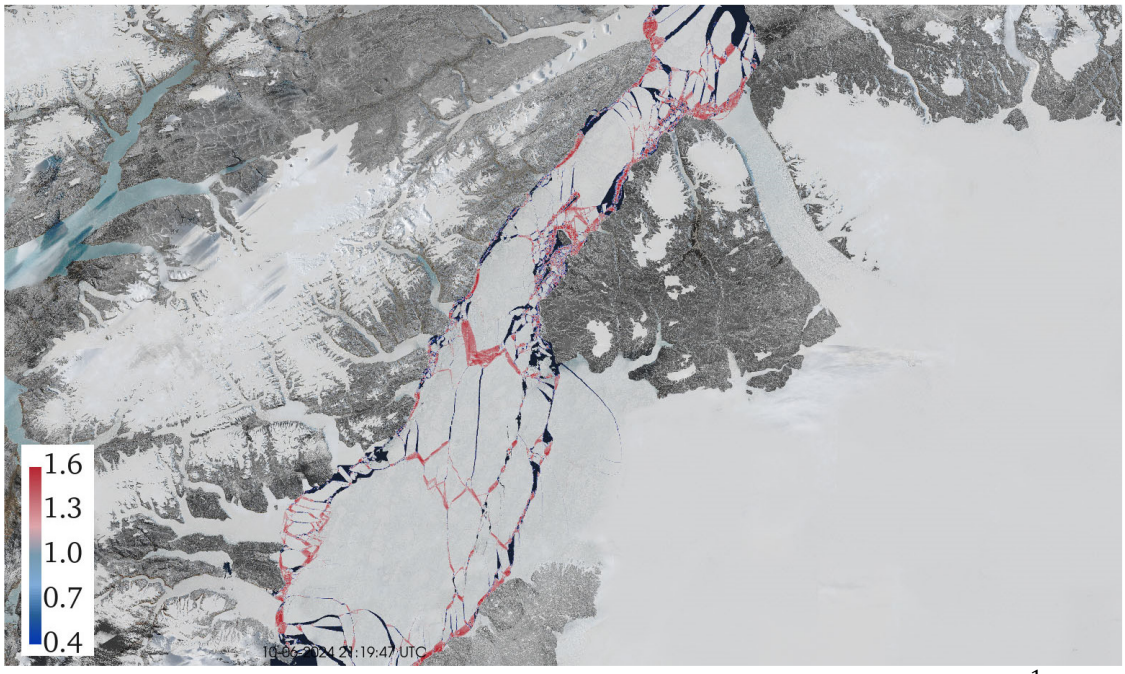

Figure 6. Simulation results after 18 hours, full region. Relative surface density J_p^{-1} is indicated in color. Red areas correspond to ridge formation whereas traces of blue color at fracture boundaries show the expansion (dispersal) of the material.

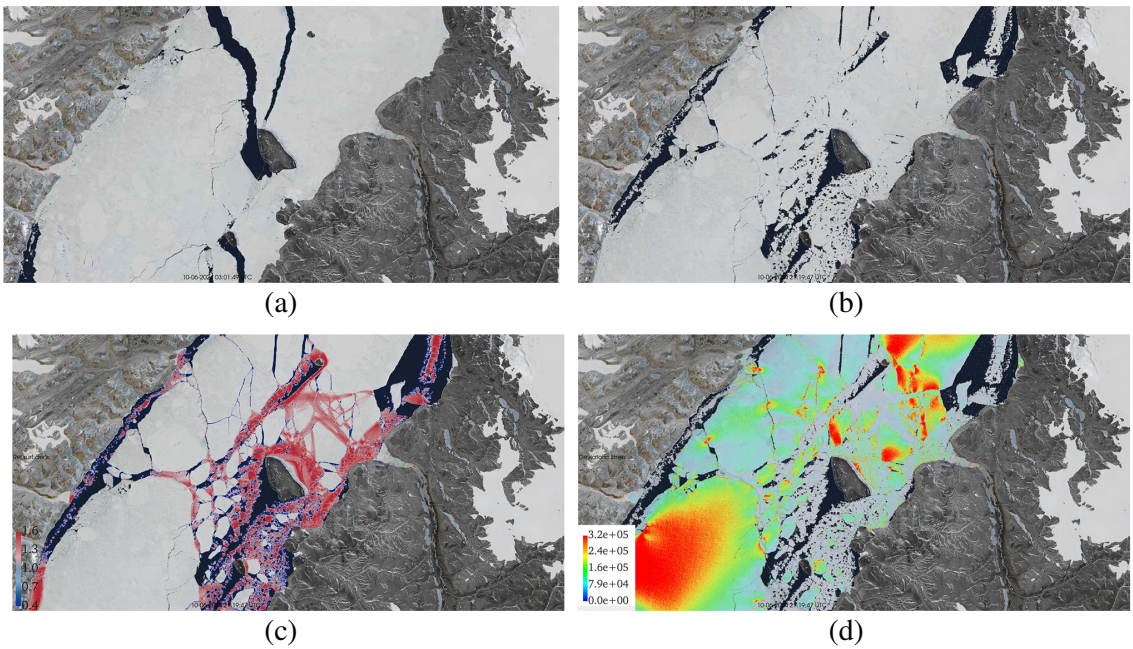

(a) (b)

(c) (d)

Figure 7. Zoom view of Hans Island, Crozier Island, and Franklin Island in Kennedy Channel. (a) Initial configuration. (b) 18 hours of the simulation. (c) Relative surface density shown in color. (d) Von Mises Stress shown in color.

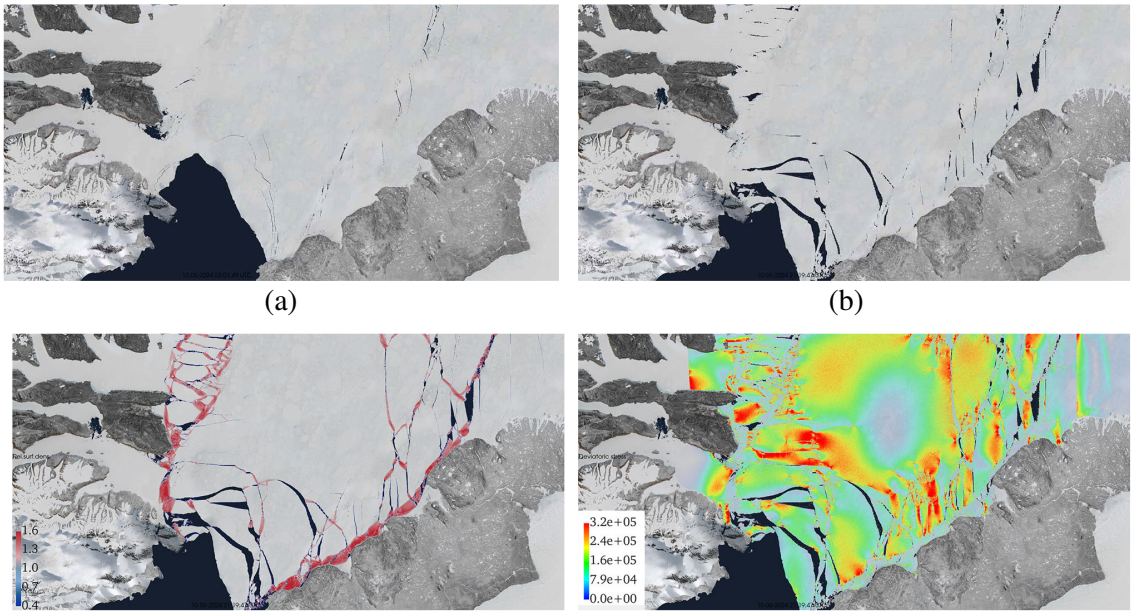

Figure 8. Zoom view of Smith Sound. (a) Initial configuration. (b) 18 hours of the simulation. (c) Relative surface density shown in color. (d) Von Mises Stress shown in color.

The fragmentation is particularly interesting in the vicinity of the three islands in Kennedy Chanel - Hans Island, Crozier Island, and Franklin Island. In the pre-computed steady flow, the currents flow around the islands. The breakup of ice occurs in the areas of high shear stress, caused by the current drag of the whole sheet as well as the local changes in flow direction, especially around the islands. Figures 7a and 7b show the initial and the final simulation states. Figure 7c highlights the changes in surface density J_p^{-1}, and Figure 7d shows von Mises Stress q given by expression (5). Shear stress values as high as 1 MPa are present in the large floes, whereas the fractured material does not sustain deviatoric stress. The forces are transmitted at the contact points of colliding floes in the form of force chains (Figure 7d).

Another interesting area is where Kane Basin meets Smith Sound (Figure 8a-d). The fragmentation is caused mainly by the pressure and movement of the ice cover of the Kane Basin rather than local drag forces. Figure 8d also shows the force chains linking the adjacent floes. The highest stress concentrations are at the contact points of the fragments. In comparison with the breakup in Kennedy Channel (Figure 7c), there is more intact material and fewer ridges since the ice cover is more likely to fracture in shear rather than accumulate in front of an obstacle.

DISCUSSION

The loading forces in the simulation are greatly simplified in comparison with the natural conditions around the same dates. The simulation assumes a steady current with a relatively high drag coefficient, meaning that the ice cover is forced to fracture and move with the flow. In nature, a combination of wind and current is responsible for the breakup. As a result, the ice does not move as far along the strait, but the changes in wind and current direction cause higher levels of fragmentation. Cloud-free satellite images are available, for example, for June 17, 2024 (Figures 9a, 9b).

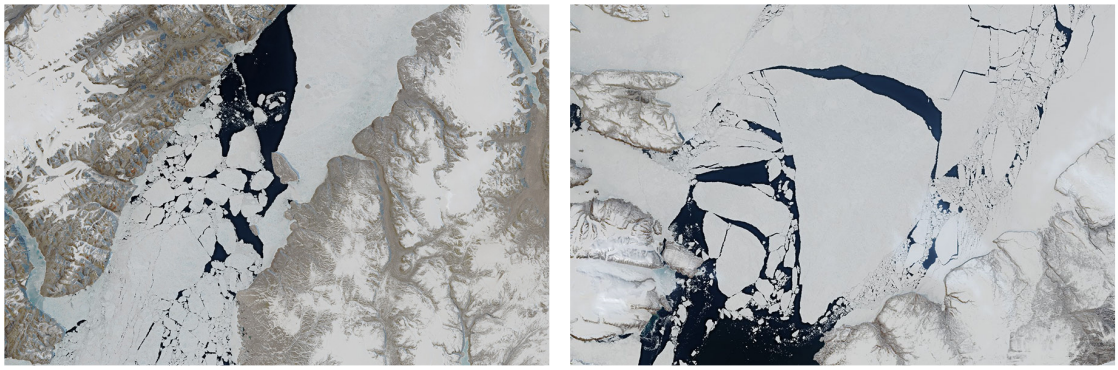

(a) (b)

Figure 9. Sentinel-2 images taken on June 17, 2024. (a) Islands area. (b) Smith Sound. ("Copernicus Sentinel-2 satellite imagery," 2024)

Near the islands (Figure 9a), the fracture pattern significantly differs from the simulation, as it is mainly caused by the alternating wind and current direction (whereas in the simulation, the breakup is caused by the steady current). At Smith Sound, however, the simulation shows more similarity with the natural pattern since the breakup occurs due to the stress in the ice sheet. It should be noted that the images were taken on June 17, 2024, approximately one week after the start of the breakup on June 10, 2024. Whereas in the simulation, only an 18-hour period is considered.

The current model has several simplifications, which should be refined in future work. Currently, relative surface density J_p^{-1} is capped by a constant value, selected somewhat arbitrarily. It would be physically meaningful to set a relationship between the ridge height and the local pressures during compression stage. Such a relationship exists, as thicker and taller ridges are associated with higher pressures.

Application of the drag force is another area for improvement. In MPM, external forces are applied at the grid update step (Figure 2) of the simulation cycle by modifying the momentum of the grid nodes. A common formulation for water or wind drag force on sea ice assumes that the force is quadratically proportional to the relative velocity between the ice and the fluid:

$$F_{\text{cell}} = \rho_a C \mathbf{v}^2 h^2, \tag{8}$$

where ρ_a is the fluid density, C is the drag coefficient, $\mathbf{v}$ is the relative velocity vector, and h is the size of the grid cell. Implementing this approach with an explicit integration scheme can cause numerical instability by violating the Courant-Friedrichs-Lewy condition. In the Material Point Method, during the particle-to-grid (P2G) step, some grid nodes may receive very little mass if particles barely influence them. When forces are applied to these low-mass nodes, the resulting acceleration can become extremely large, leading to unstable velocity updates. In our case, the simulation stopped after 18 hours of simulated time due to such an instability. One solution is to formulate the drag forces differently, ensuring that the added impulse is within acceptable limits.

CONCLUSIONS

The Material Point Method (MPM) is a promising approach for modeling the dynamics and fragmentation of ice sheets, leveraging GPU-accelerated simulations to handle per-point and

per-cell calculations. This study establishes MPM's capability to represent ice motion and breakup under simplified conditions, providing a framework for analyzing stress distributions and their potential implications for ice cover behavior. However, the current implementation is constrained by several limitations. The forcing is limited to a static water drag scenario and does not account for other environmental factors like tidal currents and wind, which are critical to real-world ice dynamics. Additionally, the model operates at a 29-meter grid resolution, while satellite imagery, available at a 10-meter resolution, reveals finer details not captured in the simulation.

Comparison with satellite observations further highlights discrepancies: while the imagery indicates greater fragmentation, it suggests less overall ice motion than simulated. Conducted on desktop hardware, the simulations also face practical constraints in resolution and computational efficiency, underscoring the need for enhanced resources. Despite these shortcomings, the method demonstrates potential for scientific application. For instance, stress estimates derived from MPM could clarify the mechanical response of ice to navigation channels. The method may forecast the probabilistic tracking of ice floe drift, though precise fracture geometries remain unpredictable. The approach may be applicable in other contexts, such as river ice breakup or the inclusion of creep and refreezing. Overall, the modelling method could refine our understanding of ice dynamics and its interactions with atmospheric and oceanic systems.

This work serves as an exploratory step in applying MPM to ice sheet modeling, revealing both its strengths and areas requiring development. Future research should focus on integrating realistic loading scenarios, improving resolution through advanced computational platforms, and incorporating direct measurements of ice properties to better align simulations with observational data. Such advancements would strengthen MPM's capacity to contribute to the quantitative study of ice mechanics.

ACKNOWLEDGEMENTS

This work was supported by the Japan Society for the Promotion of Science (JSPS) through a JSPS postdoctoral fellowship #P24720.

REFERENCES

Åström, J., Robertsen, F., Haapala, J., Polojärvi, A., Uiboupin, R., Maljutenko, I., 2024. A large-scale high-resolution numerical model for sea-ice fragmentation dynamics. The Cryosphere 18, 2429–2442. https://doi.org/10.5194/tc-18-2429-2024

Copernicus Sentinel-2 satellite imagery [WWW Document], 2024. . Eur. Space Agency. URL https://browser.dataspace.copernicus.eu (accessed 3.6.25).

Derradji-Aouat, A., 2003. Multi-surface failure criterion for saline ice in the brittle regime. Cold Reg. Sci. Technol. 36, 47–70. https://doi.org/10.1016/S0165-232X(02)00093-9

Derradji-Aouat, A., 2000. A unified failure envelope for isotropic freshwater ice and iceberg ice. Presented at the ASME/OMAE-2000, Int. Conference on Offshore Mechanics and Arctic Engineering, Polar and Arctic section, New Orleans, USA.

European Union-Copernicus Marine Service, 2020. Arctic Ocean Physics Reanalysis. https://doi.org/10.48670/MOI-00007

Haas, C., Beckers, J., King, J., Silis, A., Stroeve, J., Wilkinson, J., Notenboom, B., Schweiger, A., Hendricks, S., 2017. Ice and Snow Thickness Variability and Change in the High Arctic Ocean Observed by In Situ Measurements. Geophys. Res. Lett. 44. https://doi.org/10.1002/2017GL075434

Hu, Y., Fang, Y., Ge, Z., Qu, Z., Zhu, Y., Pradhana, A., Jiang, C., 2018. A moving least squares material point method with displacement discontinuity and two-way rigid body coupling. ACM Trans. Graph. 37, 1–14. https://doi.org/10.1145/3197517.3201293

Kirillov, S., Babb, D.G., Komarov, A.S., Dmitrenko, I., Ehn, J.K., Worden, E., Candlish, L., Rysgaard, S., Barber, D.G., 2021. On the Physical Settings of Ice Bridge Formation in Nares Strait. J. Geophys. Res. Oceans 126, e2021JC017331. https://doi.org/10.1029/2021JC017331

Kwok, R., 2005. Variability of Nares Strait ice flux. Geophys. Res. Lett. 32, 2005GL024768. https://doi.org/10.1029/2005GL024768

Kwok, R., Toudal Pedersen, L., Gudmandsen, P., Pang, S.S., 2010. Large sea ice outflow into the Nares Strait in 2007. Geophys. Res. Lett. 37, 2009GL041872. https://doi.org/10.1029/2009GL041872

Lange, B.A., Haas, C., Charette, J., Katlein, C., Campbell, K., Duerksen, S., Coupel, P., Anhaus, P., Jutila, A., Tremblay, P.O.G., Carlyle, C.G., Michel, C., 2019. Contrasting Ice Algae and Snow-Dependent Irradiance Relationships Between First-Year and Multiyear Sea Ice. Geophys. Res. Lett. 46, 10834–10843. https://doi.org/10.1029/2019GL082873

Moore, G. W. K., Howell, S. E. L., & Brady, M. (2023). Evolving relationship of Nares Strait ice arches on sea ice along the Strait and the North Water, the Arctic's most productive polynya. Scientific Reports, 13(1), 9809.

Nguyen, V.P., Vaucorbeil, A.D., Bordas, S., 2023. The Material Point Method: Theory, Implementations and Applications, Scientific Computation. Springer International Publishing, Cham. https://doi.org/10.1007/978-3-031-24070-6

Polojärvi, A., 2022. Numerical model for a failure process of an ice sheet. Comput. Struct. 269, 106828. https://doi.org/10.1016/j.compstruc.2022.106828

Wolper, J., Gao, M., Lüthi, M.P., Heller, V., Vieli, A., Jiang, C., Gaume, J., 2021. A glacier–ocean interaction model for tsunami genesis due to iceberg calving. Commun. Earth Environ. 2, 130. https://doi.org/10.1038/s43247-021-00179-7